

www.afm-journal.de

Interfacial-Strain-Controlled Ferroelectricity in Self-Assembled BiFeO₃ Nanostructures

Jingfeng Song,* Shihao Zhuang, Michael Martin, Luis A. Ortiz-Flores, Binod Paudel, Dmitry Yarotski, Jiamian Hu, Aiping Chen, and Bryan D. Huey

Self-assembled BiFeO₃-CoFe₂O₄ (BFO-CFO) vertically aligned nanocomposites are promising for logic, memory, and multiferroic applications, primarily due to the tunability enabled by strain engineering at the prodigious epitaxial vertical interfaces. However, local investigations directly revealing functional properties in the vicinity of such critical interfaces are often hampered by the size, geometry, microstructure, and concomitant experimental artifacts. Ferroelectric switching in the presence of lateral distributions of vertical strain thus remains relatively unexplored, with broader implications for all strainengineered functional devices. By implementing tomographic atomic force microscopy, 3D domain orientation mapping, and spatially-resolved ferroelectric switching movies, local tensile strain significantly impacts the ferroelectric switching, principally by retarding domain nucleation in the BFO nearest to the vertically epitaxial tensile-strained interfaces. The relaxed centers of the BFO pillars become preferred domain nucleation and growth sites for low biases, with up to an order of magnitude change in the edge:center switching ratio for high biases. The new, multi-dimensional imaging approach—and its corresponding insights especially for directly strained interface effects on local properties—thereby advances the fundamental understanding of polarization switching and provides design principles for optimizing functional response in confined nanoferroic systems.

1. Introduction

Self-assembled vertically aligned nanocomposite (VAN) systems comprising epitaxial spinel pillars embedded in a single crystal perovskite matrix have been intensively studied over the

Prof. J. Song, M. Martin, L. A. Ortiz-Flores, Prof. B. D. Huey
Department of Materials Science and Engineering
University of Connecticut
Storrs, CT 06269, USA
E-mail: jingfeng.song@uconn.edu
S. Zhuang, Prof. J. Hu
Department of Materials Science and Engineering
University of Wisconsin-Madison
Madison, WI 53706, USA
B. Paudel, Dr. D. Yarotski, Dr. A. Chen
Center for Integrated Nanotechnologies (CINT)
Los Alamos National Laboratory
Los Alamos, NM 87545, USA
The ORCID identification number(s) for the author(s) of this article

can be found under https://doi.org/10.1002/adfm.202102311.

DOI: 10.1002/adfm.202102311

with above room temperature ferromagnetism and ferroelectricity are particularly interesting for their high magnetoelectric response and tunable functionalities, with promising applications to logic and memories.[10–12] For instance, previous works have demonstrated tunable microstructure and ordering,[5,14-18] magnetic anisotropy, [2,4,6–8,18] local conduction, [9] ferroelectric properties, [2,4,19] as well as electric field control of magnetism^[20,21] in self-assembled BFO-CFO nanocomposites. These functionalities have been effectively tuned by leveraging the epitaxial vertical lattice strain, a unique advantage of VANs controlled by the high fraction of interfacial area.[11,22,23] The BFO-CFO VANs in previous studies have two typical configurations. The most common type is composed of CFO nanopillars embedded in a BFO matrix, typically fabricated to control the geometry and densities of the CFO nanopillars during self-assembly,[5,14,16,17]

past decade due to their tunable electric,

magnetic and multiferroic properties.[1-13]

Among the existing VAN systems, BiFeO₃-CoFe₂O₄ (BFO-CFO) nanocomposites

strain-mediated electric-field-induced magnetization switching in the CFO nanopillars, [20,24] and enhanced local conduction at the CFO-BFO interfaces.^[9] The less common "inverse" type of VANs, with BFO nanopillars embedded in a CFO matrix, were prepared to study the growth conditions and kinetics of BFO-CFO nanocomposites, [5] and the magnetoelectric coupling of the BFO-CFO bulk heterojunction.^[25] For these BFO-CFO VANs and other similar functional VANs with a large vertical lattice mismatch, there are few experimental reports investigating how the mismatch strain at the vertical CFO/BFO interface and its possible relaxation affects the ferroelectric switching and associated functional properties in the laterally clamped BFO nanopillars.[13,26,27] Instead, research into strain effects on ferroelectricity for BFO has mostly been limited to the case of continuous thin films, [2,3,11,13,28–33] where the mismatch strain arises from the planar film/substrate interface. Since the dimensionality hinders most direct measurements of the resulting local materials properties, the nanoscale influence of strain effects is primarily surmised from macroscopic measurements or purely microstructural analysis. [30,31,33–35] Therefore, to overcome these limitations, we designed VANs with unique (001)-oriented BFO



www.afm-journal.de

nanopillars of higher molar ratio embedded in a CFO matrix. This inverse design is distinct from previous investigations on CFO as isolated nanostructures embedded in a surrounding high molar ratio BFO matrix, [1,2,4,5,7-9,15-21,36] and also different from previous works on (111)-oriented, lower molar ratio BFO pillars in a CFO matrix. [37] Given recent demonstrations of topological polarization states and other unique functionalities in geometrically-confined nanostructures, [38-42] direct evidence for strain-induced interfacial effects on ferroelectricity is important both fundamentally, and for future applications of vertically aligned functional nanocomposites, and other strain engineered devices.

Piezoresponse force microscopy (PFM) is an essential tool for studying ferroelectric properties of such systems with nanoscale spatial variations.[1,2,4-9,14,16-21,38,39,43,44] For ferroelectric switching of BFO-CFO VAN systems, however, only one or a few local hysteresis loops are typically measured, usually by "parking" a conductive atomic force microscopy (AFM) probe at single or arrayed points in BFO, sweeping the tip-sample bias, and recording the resulting changes in the piezoresponse.[2,4,11,15–18,28,38] Single-point hysteresis measurements can be challenging to interpret, though, due to the superposition of piezoelectric effects and electrostatics[45] or ionic motion.[46] Topographic crosstalk is another persistent concern due to sensitivities to the tip-sample contact area, especially when the surface morphology exhibits changes in slope or curvature with length scales equivalent to the dimensions of the tip apex.[47] This can be exacerbated by the unique two-phase structure of the VAN systems, where the as-grown thin films normally exhibit a rough surface, including facets, interfacial grooving, and even apparent "extrusions" up to 40-100 nm above the surface for the matrix or pillar phases. [2,4-6,9,14-17,38,39] Finally, the prodigious interfacial area for VANs, along with corresponding strain gradient heterogeneities, essentially necessitates a statistical analysis of high-fidelity maps of ferroelectric polarization and switching in order to thoroughly understand and hence improve engineered interfacial coupling.

Accordingly, we implement our unique tomographic atomic force microscopy (T-AFM) approach, [48–51] leveraging the in situ nanomachining and especially surface smoothing capability,[50] for high-resolution piezoresponse mapping with negligible topographic artifacts. This enables the first nanoscale 3D map of ferroelectric domains throughout a multifunctional nanocomposite thin film. For a fixed sample thickness, alternating conventional PFM scans with sequentially increasing DC biases separately provides movies of domain switching for spatially resolving hysteresis loops and nucleation events.^[52] For highly ordered, ≈50 nm tall BFO nanopillars, epitaxially confined vertically by a surrounding CFO matrix with a slightly higher lattice parameter, a tensile strain is imposed on the outer shell of BFO pillars. For pillars with sufficiently large lateral size, this tensile strain would relax away from the edges, such that their cores can exhibit properties that are similar to epitaxial BFO thin films. Correspondingly, through high fidelity imaging and statistical analysis with up to 9.44 million voxels and 2.16 million pixels, we found that coercive voltages and nucleation dynamics of BFO nanopillars are all significantly impacted by interface proximity—in this case, up to a radial separation of 30-50 nm. The acquisition and associated data mining of such nanoscale, 3D resolved piezoresponse maps for VANs thereby contributes a new perspective on strain-engineered ferroelectricity, with fundamental and practical implications especially for future devices that leverage the independent as well as emergent benefits of functional nanocomposites.

2. Results and Discussion

The self-assembled nanopillars of (001)-oriented rhombohedral BFO were grown epitaxially among a matrix of (001) spinel CFO, on a conducting Nb-doped SrTiO3 (STO) (Nb:STO) substrate using pulsed laser deposition. Reciprocal space mapping and X-ray diffraction (XRD) spectra of the as-grown BFO-CFO nanocomposite (Figure 1a,b) indicate two regions of different strain status for the BFO nanopillars and uniform strain for the CFO matrix. By using multiple-peak-fitting approach on the experimental XRD spectra (gray curve in Figure 1b), we are able to resolve individual peaks for the strained CFO matrix (dark blue curve), strained BFO (red curve), and relaxed BFO (cyan curve).^[53] Based on the lattice parameters calculated from these fitted curves, we extract an out-of-plane compressive strain of -2.67% for the CFO matrix, and an out-of-plane tensile strain of 1.86% for the outer shells of the BFO nanopillars, and a slightly compressive out-of-plane strain of -0.12% for the cores of BFO nanopillars (Section S1, Supporting Information). Since the (001) Nb:STO substrate typically induces out-of-plane tensile strain on epitaxial (001) CFO, the measured out-of-plane compressive strain of -2.67% in the CFO matrix is attributed to the lattice mismatch at the vertical CFO/BFO interface. This outof-plane compression in one phase and tension in another is consistent with previous results of many other VANs.[13] Note that the possible contribution of thermal stress to this -2.67% out-of-plane compressive strain in the CFO matrix is ruled out given the relatively small differences in the thermal expansion coefficients of the BFO (6.83–12.8 \times 10⁻⁶ K⁻¹), CFO (11.8 \times $10^{-6}~{\rm K}^{-1}$) and STO (8.7 \times $10^{-6}~{\rm K}^{-1}$).[54–58]

For high fidelity imaging of ferroelectric domains and switching characteristics with negligible topographically induced artifacts, it is crucial to minimize surface roughness.^[47] We achieve this via nanomachining with the AFM probe itself,^[50] as is illustrated in Figure 1c. Unlike conventional lowload AFM studies with VANs,[2,4,16,17,19,38,39,59] this approach employs downforces as high as μ Ns with a diamond-coated probe during scanning, and effectively polish the as-grown rough surface. High-resolution topography and functional properties (piezoresponse, electrical conductivity, etc.) can then simultaneously or sequentially be mapped. [50,51] The as-received BFO-CFO nanocomposite surface exhibits a root-mean-square (RMS) roughness of 16.8 nm, up to 80 nm protrusions of the CFO, and growth-related grooving at the interfaces as deep as 30 nm (Figure 1d). On the CFO matrix, there are also some rounded CFO nanostructures protruding as high as 200 nm at certain intersections of differently aligned CFO "walls" (marked with white dashed circles in Figure 1d) (see Section S2, Supporting Information). Following nanomachining, however, the RMS roughness diminishes by more than an order of magnitude to 1.4 nm (Figure 1e). This is especially clear in the almost featureless corresponding deflection image which is principally

www.afm-journal.de

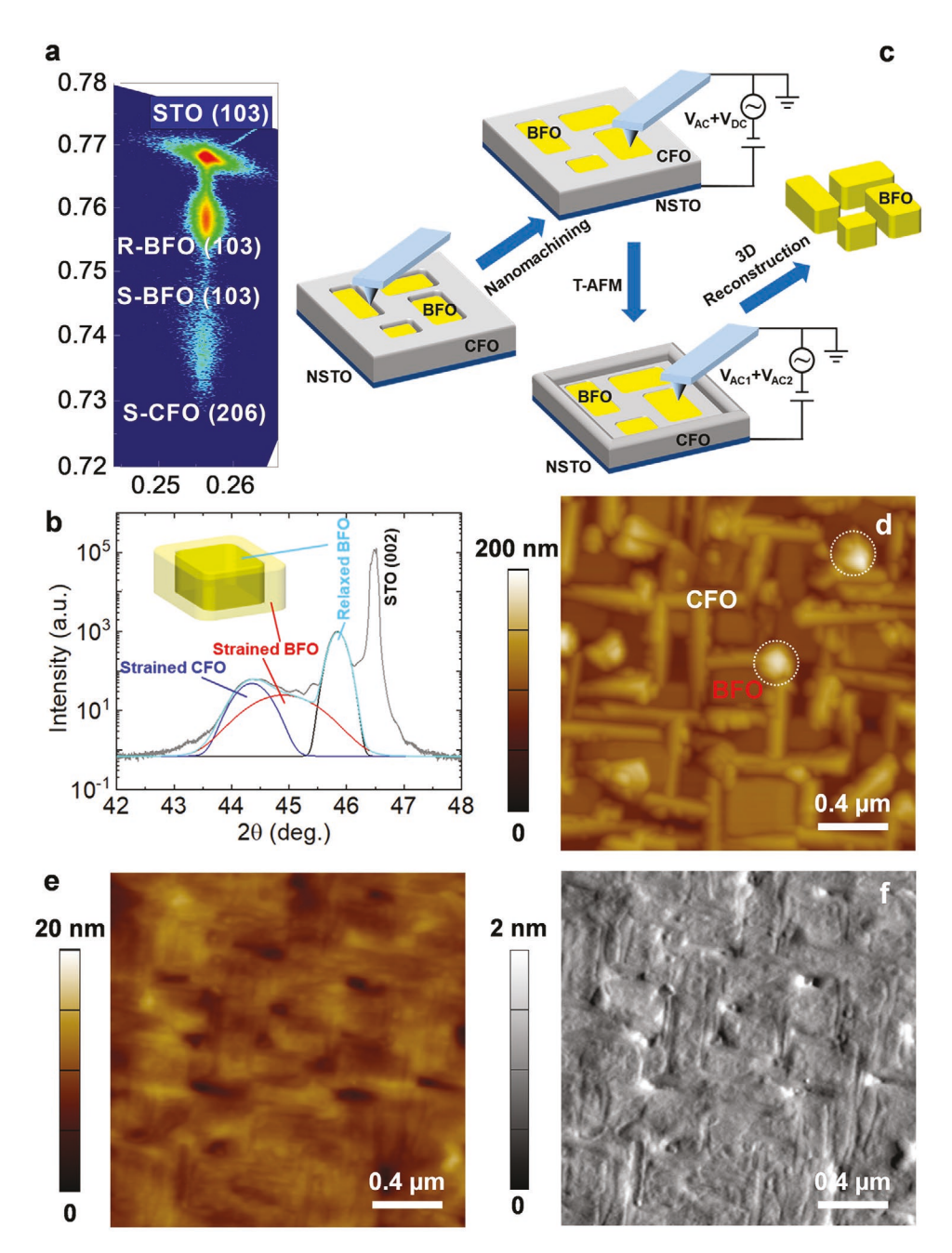


Figure 1. Structural characterization and nanomachining of BFO-CFO nanocomposite thin film. a,b) RSM and XRD ω-2 θ scan of as-grown BFO-CFO VAN. The strained BFO (S-BFO, red curve), relaxed BFO (R-BFO, cyan curve), and strained CFO (S-CFO, blue curve) have been indicated, respectively. c) Schematic illustration of the three key experimental procedures in this study: nanomachining of as-received BFO-CFO thin film, PFM sequential switching, and imaging on the significantly polished interfaces, followed by T-AFM, and finally 3D reconstruction of the isolated BFO nanopillars. d) AFM topography of the as-received BFO-CFO surface with RMS roughness of 16.8 nm due to the CFO extrusions above the BFO-CFO interfaces. The white dashed circles mark some rounded CFO nanostructures protruding as high as 200 nm at certain intersections of differently aligned CFO "walls". e,f) The AFM topography and deflection images of the BFO-CFO nanocomposite surface after nanomachining around 10 nm beneath the as-grown surface plane. The RMS roughness is reduced ten-fold to 1.4 nm. The deflection signal, which is particularly sensitive to small surface fluctuations, is reduced to less than 2 nm.

sensitive to edges (Figure 1f). Crucially, although the film has been mechanically eroded, the damage to the properties of the underlying material is negligible according to prior PFM and cross-sectional transmission electron microscopy for homogeneous BFO thin films thinned to lower than 10 nm. [48]

By extending this concept through repeated high-load nanomachining as well as simultaneous property mapping, the BFO-CFO VAN films are progressively milled and measured to enable T-AFM. In fact, two superimposed AC sinusoidal biases are applied to the tip, corresponding to the 1st www.advancedsciencenews.com www.afm-journal.de

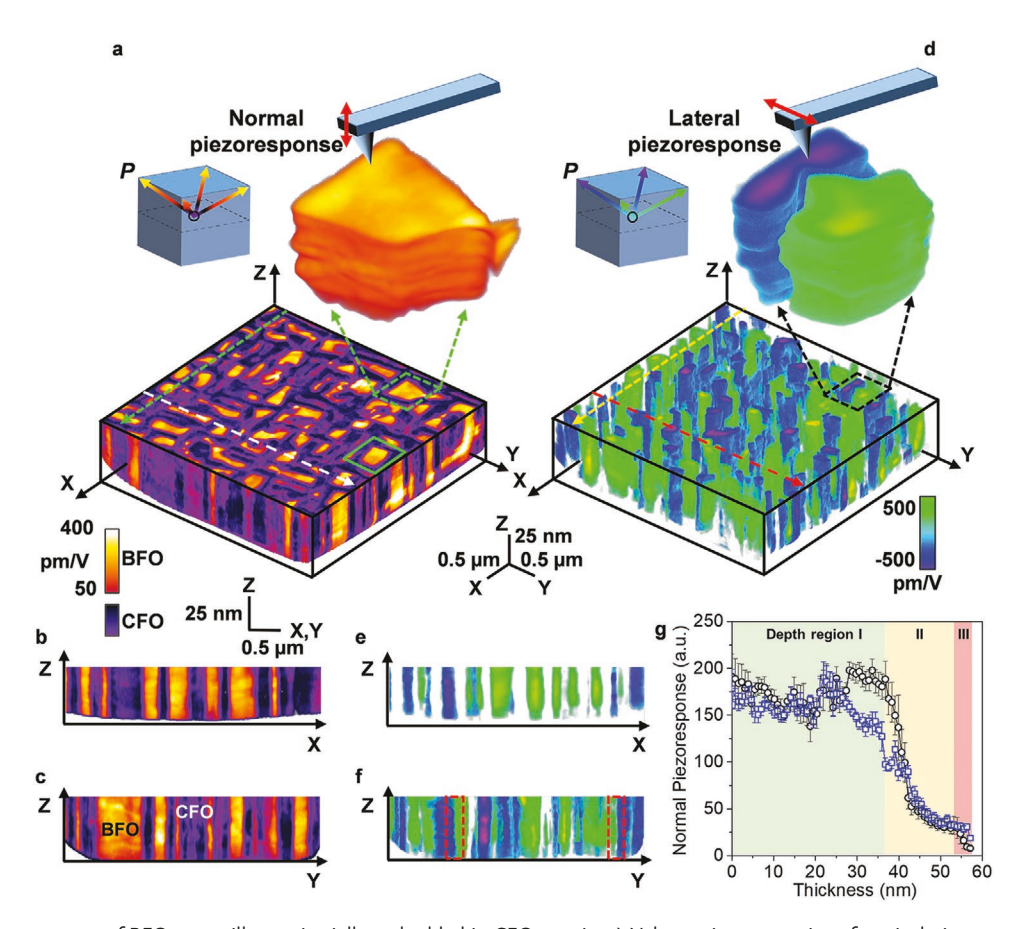


Figure 2. 3D piezoresponse of BFO nanopillars epitaxially embedded in CFO matrix. a) Volumetric perspective of vertical piezoresponse of BFO-CFO nanocomposites, with strong contrast for BFO and a negligible signal (different color scheme) for CFO. b,c) Tomographic cross-sections of the vertical piezoresponse along dashed overlays from (a), respectively for the xz and yz planes. d) Volumetric perspective of lateral piezoresponse of BFO nanopillars only. CFO regions have been computationally removed to better distinguish domains aligned oppositely along $\pm y$ directions. e,f) Tomographic cross-sections of the lateral piezoresponse for the same xz and yz planes as in (b,c). Magnified vertical and lateral tomograms for a single polydomain nanopillar are displayed as insets (top) along with schematics clarifying the probe alignment and polarization vector sensitivity. The possible polarization orientations with respect to different color schemes in the tomograms are also listed next to each tomogram respectively. g) Depth-dependent normal piezoresponse profiles averaged over individual BFO nanopillars. The black (blue) curve corresponds to green solid (dashed) box marked in a. Three depth regions are identified (marked with I, II, and III respectively).

normal and torsional cantilever resonances, over hundreds of images until the underlying Nb:STO substrate is reached. In this manner, independent image sequences for the vertical (z-axis) and lateral (y-axis) piezoresponse, amplitude \times cos (phase), are calculated in post-processing for each of these spectrally distinct signals. Finally, in Figure 2, complementary normal and lateral tomograms with rectilinear voxels are reconstructed for 3D analysis and rendering. The vertical and lateral piezoresponse tomograms in Figures 2a,d, respectively, each comprise almost 10 million voxels. Figure 2b,c reveals the cross-section tomograms from locations indicated in Figure 2a, which indicate a strong vertical PFM response associated with the BFO nanopillars, with negligible piezoresponse from the non-ferroelectric CFO matrix.^[4] Moreover, the highly columnar microstructure and nanopillar shape of BFO is confirmed throughout the measured thickness, consistent with high-quality epitaxial growth (Figure 1) and additional tomographic analysis (Section S10, Supporting Information). These observations are well-supported in the lateral piezoresponse tomograms in Figures 2d-f, where the CFO phase has been

computationally removed for visual clarity. The color contrast in Figures 2d–f thereby displays oppositely oriented in-plane polarization vectors within the BFO only (along the $\pm \gamma$ axis as sketched in Figure 2d). It is clear that some nanopillars support multiple lateral domains, with primarily vertical domain walls as indicated within the overlain rectangles of Figure 2f. This is especially apparent for the magnified tomogram regions in the insets of Figures 2a,d.

According to the structural characterizations in Figure 1, the (001)-oriented epitaxial BFO nanopillars have a rhombohedral lattice symmetry. In combination with the fact that the out-of-plane (z-axis) components of the polarization are all pointing upwards, as is shown in the inserts of Figures 2a,d, there are four possible polarization directions along the <111>pc directions ("pc" means pseudocubic). [60] Because the polarizations are not perfectly aligned along the z-axis, multiple lateral domains corresponding to the in-plane polarization components would typically form to minimize the free energy of the system. [61] Other factors, such as the lateral size of the BFO pillars (around 150–300 nm) are significantly larger than the





www.afm-journal.de

VAN film thickness (≈50 nm), and the inhomogeneous strain distribution throughout the BFO pillars, could further facilitate the stabilization of multiple lateral domains. [62] From the volumetric tomograms, we are able to extract the depth-dependent of the piezoresponse of each BFO nanopillars. For instance, Figure 2g shows two typical normal piezoresponse amplitude profiles averaged over individual BFO nanopillars with respect to depth. According to the depth-dependent profiles, three regions (region I, 0-35 nm; region II, 35-52 nm; region III, 52-56 nm) are identified. Region I exhibits a relatively stable piezoresponse amplitude, with fluctuations < 15% throughout the top 75% of the BFO thickness. In region II, the piezoresponse decrease sharply up to 80% due to the clamping effect from the substrate, which has been demonstrated to reduce the piezoelectric coefficient d_{33} up to 76% in PZT thin films. [63,64] Finally, there is almost negligible piezoresponse in the last 3-5 nm of the film, region III, as the milling process reaches the non-piezoelectric Nb:STO conducting bottom electrode and substrate.

It is worth pointing out that the T-AFM approach is based on sequential PFM imaging of exposed surfaces with respect to discrete depths of the BFO-CFO nanocomposite during the AFM-tip serial sectioning procedure. [48,51] In this sense, T-AFM is different from previous non-invasive volumetric imaging methods, such as sending thermal waves from sample surface to collect signals from the interior, then use comprehensive mathematical deconvolution approach to extract depthdependent properties, including polarization, pyroelectric coefficient, etc. [65] However, T-AFM is uniquely advantageous by acquiring volumetric properties with unit-cell level depth resolution^[48] and a smallest volumetric resolution of around 120 nm³ (this work) comparing with the micron-level lateral and depth resolution with the thermal wave method through comprehensive deconvolution procedure. [65,66] Overall, such 3D tomograms correlating multiple information channels, such as vertical as well as lateral domain polarizations, are invaluable for future efforts to precisely tune the microstructure and local properties throughout multifunctional VAN's and other 3D heterogeneous functional materials.

Perhaps eclipsing the importance of domain polarization configurations within multiferroic VAN's, however, is the value in optimizing domain stability or conversely polarization switching within the epitaxial ferroelectric phase. This can be directly investigated by conducting low-load (and hence non-machining) dual AC resonance tracking PFM (DART-PFM),[67,68] especially at a region previously nanomachined to enable artifact-free, high fidelity property mapping. By interleaving such piezoresponse images with equivalent area scans during pure DC tip-biasing, specifically increasing sequentially from 0 V to ±4 V by 25 mV steps (between tip and grounded Nb:STO back electrode), ferroelectric switching can be mapped for numerous BFO nanopillars in parallel. [69] The montage of Figure 3a-j depicts a subset of the resulting piezoresponse images (following biasing as noted), revealing the normalized vertical domain magnitude and orientation during switching in both directions.

Clearly, one complete polarization switching cycle is achieved in all ≈15 BFO nanopillars within the field of view. This is confirmed both visually (Figures 3a,e,j) and statistically

based on overlapping histograms (Figure 3k-l) of the piezoresponse for the initial and final switching states during positive and negative tip biasing. More importantly, the sequential PFM switching images in Figures 3a-j can be considered as a 2D illustration of the hysteretic behavior of the BFO nanopillars, which comprise more than 35 000 simultaneously acquired PFM hysteresis loops at each image pixel (same location on a BFO nanopillar) with respect to biases in the range of ± 4 V. To further illustrate this point, Figure 3m shows two typical hysteresis loops extracted from central (red curve) and edge (blue curve) locations in one of the BFO nanopillars (marked with red and blue dots in both e and j) during the PFM switching sequences with bias sequences of 0 V \rightarrow +4 V \rightarrow 0 V \rightarrow -4 V. Such complete and generally symmetric switching behavior confirms the quality and robust ferroelectric properties of the BFO despite the epitaxial constraint within the CFO matrix. Moreover, it is noteworthy that there is scarce evidence of such a wide coercive bias window from previous studies of VANs, likely resulting from the combination of our nanomachining approach as well as our image-based (parallel) switching studies. Compared to (serially) "parking" AFM tips at individual or comprehensive arrays of locations on as-received BFO thin films and nanostructures, [2,4,5,14,16,19,38,59] here in our case the domain switching and concomitant strain evolution progresses together—an important consideration for potentially heterogeneously strained structures such as VANs, micropatterned devices or other 3D architectures.

To further investigate the impact of interfacial strain on ferroelectricity for VANs, domain switching is spatially analyzed in Figure 4 based on the full dataset from Figure 3 comprising over 2.16 million data points. From the zero-phase-crossings on the local hysteresis (e.g., Figure 3m) at each pixel of BFO nanopillars during positive tip biasing, in Figure 4a we extract and map out the 2D distributions of coercive voltages over all the BFO nanopillars in the same image region. [69] Additionally, the images of switched domains recorded after each positive bias step, which were utilized to construct Figure 4a, are shown in Figure S3, Supporting Information. Black regions of non-ferroelectric CFO are not considered here or in any other analysis herein. All domain walls within the BFO are computationally identified for every image frame and superimposed in Figure 4b with each assigned a different color according to the associated image frame (and hence tip bias) as indicated. The various switching events are summarized for all measured biases by the dual histogram of Figure 4d, based on the sums of subsumed areas for newly switched domains following every 25 mV step across the coercive voltage range. Notably, nucleated domains within approximately 50 nm of a strained BFO-CFO interface ("Edge") are distinguished from those further away which are more likely to behave like a bulk BFO film ("Center") (see Figure S2, Supporting Information). Figure 4e recasts these results for the newly switched area per bias, presenting the edge to center switching ratio after area-normalization according to the proportion of Edge:Center BFO pixels (1:1.3) radially within or beyond a 50 nm threshold from any epitaxial interface available for switching (Figure 4c). The clear conclusions from Figure 4d,e is that domain nucleation and switching at low bias occurs mostly in the relaxed "Centers" of BFO. Switching at the "Edges" of BFO is dramatically suppressed at low biases due to

www.advancedsciencenews.com www.afm-journal.de

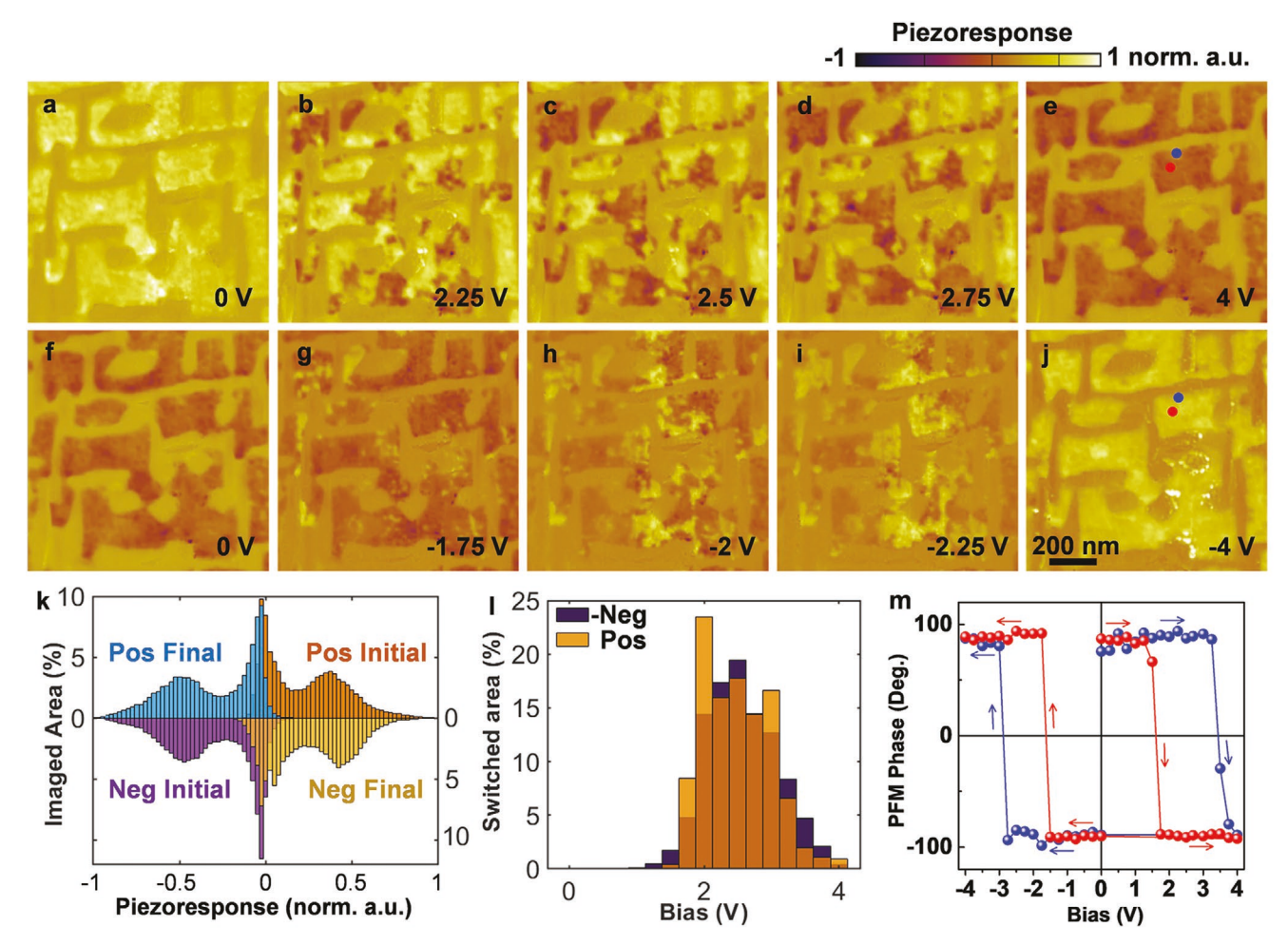


Figure 3. 2D sequential mapping of ferroelectric switching in BFO nanopillars within a 1 μ m \times 1 μ m nanomachined region. a–e) Piezoresponse montages for biases of 0, 2.25, 2.5, 2.75, and 4 V respectively. f–j) Piezoresponse montages for biases of 0, -1.75, -2, -2.25, and -4 V respectively. k) Histograms of the overall piezoresponse for initial and final polarization states bracketing each switching sequence (a and e, f and j). l) Histogram of BFO switched area with respect to applied bias. m) Typical PFM hysteresis loops extracted from central (red curve) and edge (blue curve) locations from one of the BFO nanopillars (marked with red and blue dots in e and j) through the PFM switching sequences bias of 0 V \rightarrow +4 V \rightarrow 0 V \rightarrow -4 V.

the BFO/CFO interfacial strain and becomes dominant when the applied biases are sufficiently large (>2.5 V). Analyzing the negative switching sequence (See Figure S3, Supporting Information) leads to the equivalent conclusion, that the polarization switching at the edge of the BFO nanopillars mostly occurs when the applied electric field is high enough. Moreover, with more comprehensive switching statistics, the color contrast in Figure 4f represents the log of the switched proportion of BFO with respect to the coercive voltages (abscissa) as well as the local distance to the nearest CFO interface (ordinate). Like Figures 4d,e, this confirms that domain nucleation and growth tend to be localized near strained interfaces for higher voltage magnitudes (±3.5 V for 30 nm separations according to the overlays included to guide the eye). It is noteworthy that the regions near the periphery of the analyzed area could conceivably be close to an interface that is just outside the field of view. These therefore unavoidably lead to an uncertain interfacial separation, and are ignored consequently (black in Figure 4c as compared to Figure 4a) for all analyses herein (Figure 4d-f). As a consequence of such careful, thoroughly analyzed, and

high-resolution switching studies, it is clear that engineering the BFO-CFO interface proportions and interfacial strains can significantly enhance (or diminish) the mean ferroelectric switching field strength and typically the corresponding polarization stability. Furthermore, the coercive field breadth and spatial homogeneity can equivalently be tuned. Summarizing the high fidelity PFM switching sequence and statistical analyses in Figures 3 and 4, it is concluded that: i) When the voltage bias is relatively low, polarization switching occurs only in the center region of the BFO nanopillars which possess a moderately compressive out-of-plane strain of -0.12%; ii) Only when the applied bias is sufficiently high (>2.5 V) does the polarization switching becomes appreciable and dominant at the edge near the BFO-CFO interfaces, which exhibit a large out-of-plane tensile strain of 1.86%.

Comparing our results with previous thin-film studies based on substrate-induced in-plane strain alone, the vertical tensile strain (ε_z) on the BFO nanopillars, from a strain conversion perspective, can be converted to an in-plane compressive strain ε_x based on $\varepsilon_z = v_{zx}\varepsilon_x$, where the Poison ratio v_{zx} of epitaxial

www.afm-journal.de

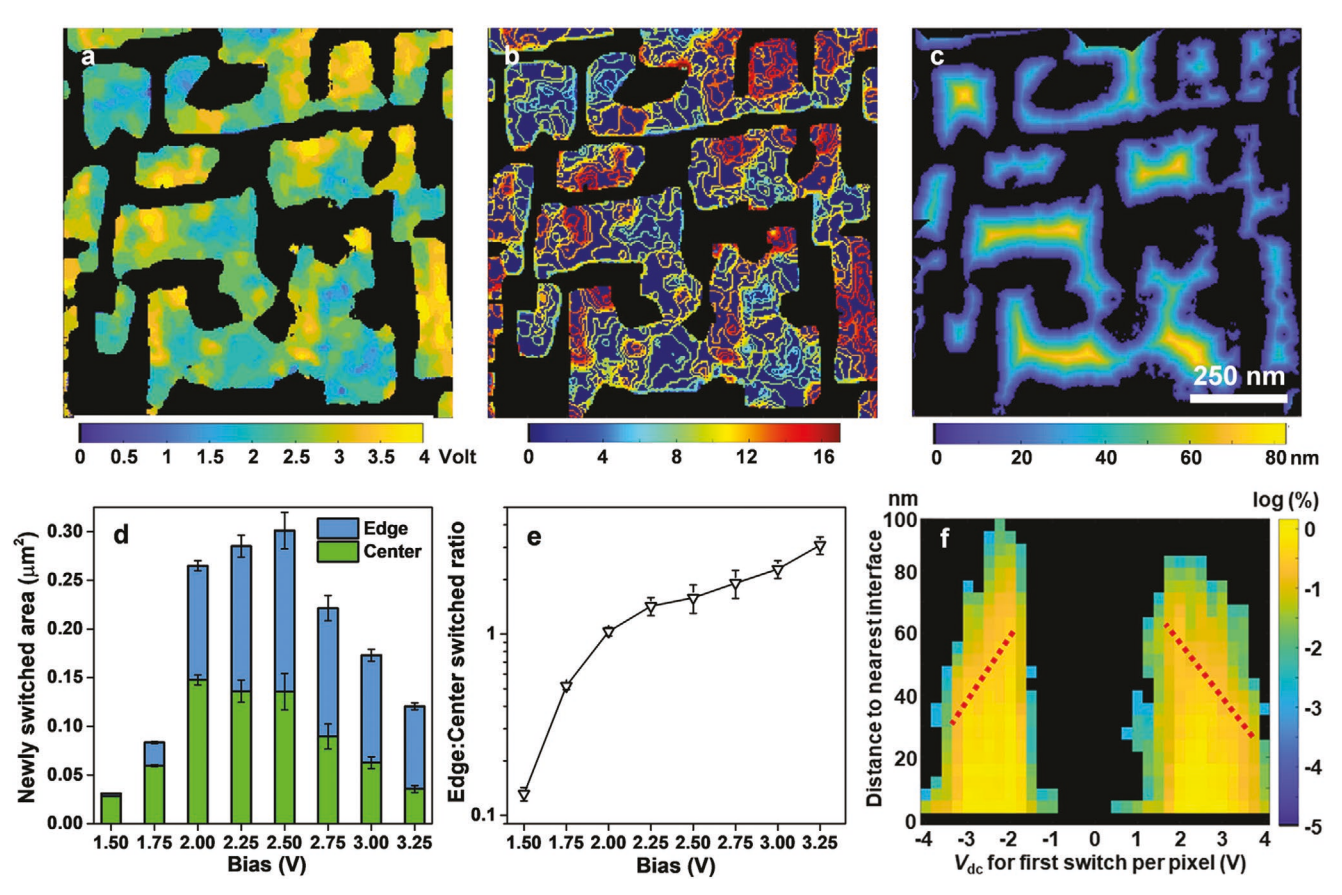


Figure 4. Spatially resolved domain switching statistics with respect to strained BFO-CFO interfaces. a) 2D mapping of BFO nanopillar positive coercive voltages per 15 nm^2 pixel during collective polarization across the field of view from Figure 3. b) Ensemble of all evolving domain wall positions throughout the switching experiment, colored by image frame. c) Certain distance to strained interfaces used for all analyses in Figure 4. In order to properly account for possible CFO interfaces beyond the field of view, compared to the raw data (a,b) several regions around the periphery are ignored (black) and hence not considered in any analysis. d) Histograms for area of newly nucleated domains as a function of increasing poling voltage, distinguished by certain radial separation from BFO-CFO interfaces ("Edge" < 50 nm < "Center"). e) Ratio of switched area for tensile-strained edges versus relaxed nanopillar centers, normalized by the relative BFO area in proximity to (within 50 nm) the nearest epitaxial CFO interface (1:1.3). f) Combined statistical analyses of the BFO coercive voltages (abscissa, V_{dc}) and switched area percentages (color scale) with respect to the distance to the nearest interface (ordinate). (a-c) share the same scale bar in (c). The error bars in (d,e) represent the uncertainties associated with categorizing switched domains located at the transition regions between "Edge" and "Center" boundaries (marked with Roman numbers in Figure S2, Supporting Information), where they may be considered as either "Edge" or "Center", and thereby are used to calculate the experimental error contributions.

BFO is around 0.3.^[70] Although it has been well-established that homogenous in-plane compressive epitaxial strain can enhance the global coercive voltage of (001) ferroelectric thin films such as BFO^[30,33] and BaTiO₃^[34,71] due to the strain-enhanced potential barrier between the two energetically equivalent polarization states, the influence of spatially inhomogeneous mismatch strains (Figure 1b) on local polarization switching (Figure 4a) in ferroelectric nanopillars embedded in an elastic matrix has hitherto remained virtually unexplored. In this sense, our result could also be essential for expanding the current observation and understanding of strain-engineered functional material systems, which are otherwise based primarily on laterally homogeneous and strain-mediated epitaxial thin film heterostructures.

Furthermore, to establish a more quantitative understanding of the influence of spatially inhomogeneous mismatch strains on polarization switching of BFO nanopillars within an elastic matrix (CFO), phase-field simulations (see Experimental Section) were performed, and the results are summarized in Figure 5.

The polarization domain structure in a single BFO nanopillar after positive out-of-plane electric field poling is shown in Figure 5a, which primarily comprises three different rhombohedral domain variants ([111]_{pc}, $[\bar{1}11]_{pc}$, and $[\bar{1}\bar{1}1]_{pc}$) separated by two 71° domain walls. The out-of-plane polarization P_z is positive in the entire BFO, which is consistent with the map of vertical piezoresponse shown in Figures 2a. The inplane polarization $P_{\rm v}$ contains both positive and negative variants, which is consistent with the map of lateral piezoresponse shown in Figure 2d. Figure 5b,c shows the corresponding distribution of out-of-plane strain $\langle \varepsilon_{zz} \rangle$ (i.e., averaging the ε_{zz} in all voxels along z) over the xy plane of the BFO and the line profile along its central transect. As shown in Figure 5b the $\langle \varepsilon_{27} \rangle$ in the edge of the BFO nanopillar is generally larger than that in the center, although $\langle \varepsilon_{zz} \rangle$ decreases sharply near the BFO/ CFO interface due to the mechanical clamping by CFO matrix. The areal average of the $\langle \varepsilon_{zz} \rangle$ (hence the volumetric average of ε_{zz}) over the entire edge region is 1.87%, which agrees well www.advancedsciencenews.com www.afm-journal.de

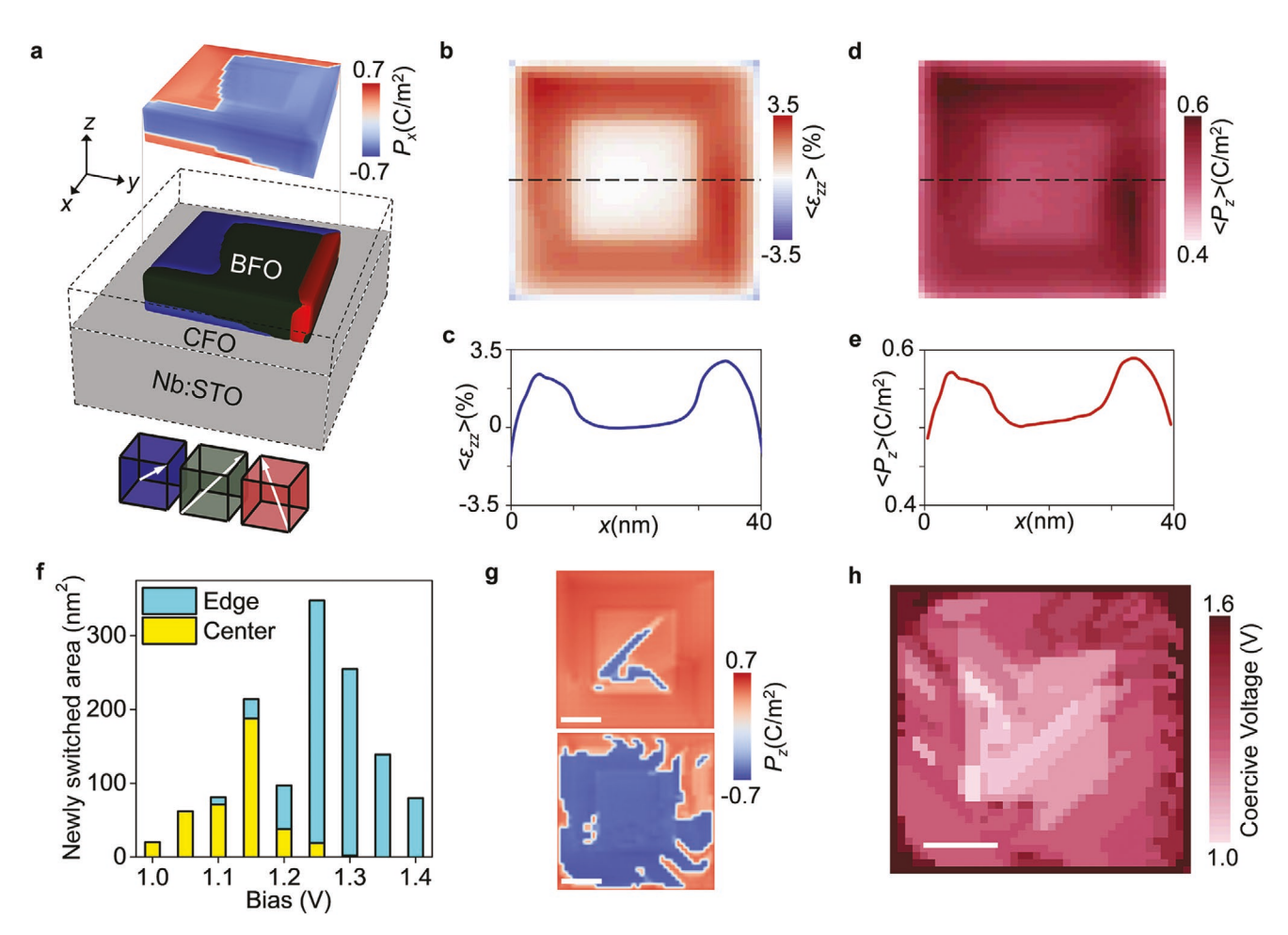


Figure 5. Phase-field simulations of polarization switching in the BFO nanopillar of the BFO-CFO VAN film. a) Polarization domain structure (lower) and distribution of in-plane component P_x (upper) at 0 V after being poled by a large electric field applied along +z. Color codes for rhombohedral variants: blue for [111]_{pc}, dark green for [111]_{pc}, and red for [111]_{pc}, b) Distribution of thickness-averaged out-of-plane strain $\langle \varepsilon_{zz} \rangle$ over the film plane and c) the line profile of $\langle \varepsilon_{zz} \rangle$ along the central transect (dashed line in (b)). d) Distribution of thickness-averaged out-of-plane polarization $\langle P_z \rangle$ over the film plane and e) the line profile of $\langle P_z \rangle$ along the same central transect (dashed line in (d)). f) Histogram for area of newly switched polarizations in center region (yellow) and edge region (cyan) as the bias voltage increases. g) Distribution of P_z on the top surface of the BFO nanopillar under a bias voltage of 1.05 V (upper) and 1.3 V (lower), respectively. h) Map of coercive voltage for polarization switching on the top surface of the BFO nanopillar. In (g,h), the scale bar is 10 nm.

with the value (1.86%) extracted from the XRD analysis. As shown in Figure 5d,e, the thickness-averaged $\langle P_z \rangle$ is also larger in the edge region and displays a line profile resembling that of $\langle \varepsilon_{zz} \rangle$. This is because larger tensile ε_{zz} in the edge of BFO tends to stabilize the polarization along the z-axis and enhance the P_z (since the electrostriction coefficient Q_{11} of BFO is positive, see Experimental Section). As a result, the coercive voltage in the edge region should also increase. For demonstration, different bias voltages were applied across the VAN film to switch the polarization domain pattern shown in Figure 5a. Figure 5f shows the simulated statistics of spatially resolved polarization switching at the surface of the BFO nanopillar, which was presented in a similar way to Figure 4d. As shown in Figure 5f, the polarization switching only occurs in the center when the voltage is relatively small (<1.1 V), and all polarizations in the center are switched down when voltage exceeds 1.3 V. This can be seen more clearly in the distributions of P_z at the top BFO surface at 1.05 and 1.3 V in Figure 5g. Moreover, the newly

switched area in the edge region first increases with voltage (1.1–1.25 V), and then decreases under higher voltages once a majority of the polarization in the edge has been flipped. Furthermore, according to coercive voltage maps of the BFO surface (in Figure 5h), the coercive voltage in the edge region is up to 1.5 times higher than that in the center. This finding also agrees well with experiments, where up to 2 times higher coercive voltage in the edge region is observed based on the PFM switching sequences (Figure 3m) and statistical analysis (Figure 4d,e).

It is worth pointing out that the defects in the vertical interfacial sites of BFO nanopillars could also facilitate the switching domain nucleation, as has been demonstrated in previous reports of low-strain or relaxed epitaxial ferroelectric PZT thin films, [72–74] where the defects such as weak random-bonds could promote nucleation by lowering the potential barrier between equivalent polarization states. [73] However, in this work, the effect of the large out-of-plane tensile strain in the edge region





www.afm-journal.de

of BFO nanopillars-which raises the potential barrier of polarization switching and hence the coercive voltage-outweighs the potential-barrier-lowering effect of the interfacial defects. [71] Additionally, although previous studies by Han et al., of geometrically-confined BFO nanoislands have demonstrated stable polar topological states with exotic center-type domains and resistive switching behavior, [41,42] no clear center-type domains, resistive switching, or charged domain walls were observed in our BFO nanopillars according to the PFM tomograms (Figure 2) and C-AFM results (Figure S1, Supporting Information). This could be due to the completely different BFO-CFO composite sample structure and epitaxial growth conditions from the previous self-assembled BFO nanoislands grown directly on BFO thin film matrices.[39,41,42] Also, the semiconducting characteristics of the CFO matrix (Figure S1, Supporting Information), and/or the interfacial strain, could destabilize the polar topological states for our VANs. More generally, given the capability to directly map polarization orientations in 3D as demonstrated in this work, T-AFM can be a powerful tool to visualize polar topological states and their corresponding exotic properties. Especially, investigating 3D conductive domain walls for ferroelectric thin films, nanocomposites, or isolated nanostructures are recommended as the next steps given the already-demonstrated ability to map local conductivity in three dimensions.[50]

Finally, our approach and findings may also provide useful guidance for optimizing the functional properties of VAN and other heterogeneous strain systems. For instance, according to the T-AFM result in Figure 2g, for BFO-CFO nanocomposite thin films, an overall thickness above 20 nm is beneficial for optimizing the piezoresponse of BFO pillars by reducing the substrate clamping effect. In terms of the lateral size of BFO pillars, the statistical analysis in Figure 4f suggests that a 30-50 nm lateral shell (edge region) near the BFO-CFO interface can be significantly impacted by the interfacial strain. Moreover, from the size-dependent phase-field simulation results on ferroelectric switching in BFO nanopillars (Section S9, Supporting Information), reducing the BFO lateral size enables an overall more uniform strain distribution and polarization switching behavior at the expense of higher local coercive voltages (Figure S8e-h, Supporting Information).

3. Conclusions

In summary, by applying the T-AFM approach to a BFO-CFO epitaxial nanocomposite with BFO nanopillars embedded in a CFO matrix, we have reached the following conclusions: 1) the T-AFM approach, which visualizes the 3D piezoresponse of BFO nanopillars volumetrically at nanoscale, is a unique and powerful tool for revealing the volumetric and depth-dependent properties underneath the as-grown surface such as piezoresponse and substrate clamping effect. Especially for multi-phase functional composites, the T-AFM can be utilized to reconstruct the volumetric distribution and properties of discrete nanophase based on their different properties (e.g., polarization, electrical conductivity, photoconductivity, etc.). 2) The AFM-tip-based nanopolishing during T-AFM has proved to be an effective process for preparing smooth surfaces essential

for acquiring high-fidelity scanning probe microscopy property maps by minimizing topographical artifacts. 3) The nonconventional VAN with BFO nanopillars embedded in a CFO matrix permits microscopic investigation of the individual or collective polarization nucleation, switching, and associated functional responses in a ferroelectric nanostructure embedded in an elastic matrix, notably the effects of spatially inhomogeneous epitaxial strains from the vertical BFO/CFO interface. Therefore, the result of this study, such as the depth-dependent properties and lateral-size-dependent effect, can provide practical design recommendations to optimize ferroelectricity in future VAN or other 3D heterogeneous strain-engineered functional devices. Finally, ongoing and future studies, such as inspecting the application of magnetic field to further tune the ferroelectricity of BFO nanostructures via the strain-mediated magnetoelectric coupling[75] could provide even further insight and optimization to the BFO-CFO VAN systems and related 3D structured materials.

4. Experimental Section

Epitaxial BFO-CFO VAN films with a thickness of 50 nm were grown on conducting single-crystal Nb-doped SrTiO $_3$ (Nb:STO) (001) substrates at 650 °C in 50 mTorr of oxygen by pulse laser deposition. The system used a KrF excimer laser with a uniform laser energy density of 2.0 Jcm $^{-2}$. The film growth target comprised uniformly mixed BFO:CFO with a molar ratio of 67:33, fixed 6.0 cm from the target. The films were in situ annealed at 400 °C in 500 Torr oxygen for 30 min, before cooling down to room temperature at 5 °C min $^{-1}$.

All AFM measurements were performed in an Asylum Research Cypher system. To nanomachine a smooth surface (Figure 1) or for full T-AFM (Figures 2), conductive-diamond-coated probes (Nanosensors CDT-NCHR) were employed during scanning with a typical setpoint of $2.8 \mu N$. The downward forces utilized with the diamond-coated probe did not alter the inherent or original states of the BFO nanopillars (Section S11, Supporting Information) For Figure 2, 821 consecutive images with 512 \times 512 pixel resolution were acquired over a 4 μm \times 4 µm area, gradually machining the surface to continually expose the underlying VAN film through to the substrate (material removal as thin as single unit cells have been demonstrated in some cases^[48]). These results, comprising 215 million total pixels, were reconstructed into 9.44 million rectilinear voxels of 7.8 nm \times 7.8 nm \times 2 nm (x,y,z) which together encompass 1.12 μm^3 of excavated film. Any nonlinear serial sectioning during T-AFM was accommodated by interpolation into gridded voxels.^[50] As shown in Figure S4, Supporting Information, more than 88% of all voxels were based on one or more real data points that were radially within 1 nearest neighbor voxel distance (11 nm) and 99.8% were within only 3 nearest neighbor voxels (33 nm).

Domain polarization vectors were mapped using a dual-frequency external lock-in amplifier (Zurich Instruments HF2LI) to apply AC biases between a conducting probe and a grounded substrate, thereby causing local piezoactuation at the bare film surface beneath the scanning AFM tip via piezo force microscopy. The dual-lock-in setup enables pixel-by-pixel detection of the vibratory amplitude and phase for both the normal piezoresponse (to resolve the out-of-plane component of converse piezoelectricity), and in some cases also the simultaneous in-plane piezoresponse based on spectrally distinct torsional cantilever resonances (Figure 2). The normal and lateral driving amplitudes were each 1 V and the frequencies were 2 MHz and 2.7 MHz respectively.

Sequentially increasing DC voltages (±25 mV per image) were additionally added to the AC tip bias for spatially resolved ferroelectric switching studies according to the normal piezoresponse (Figures 3,4). Such ferroelectric switching movie measurements were performed with a lower, non-machining setpoint force of 25 nN, using a Ti/Ir coated



www.afm-journal.de

probe (Bruker SCM-PIT) with 75 kHz resonant frequency and 2.8 Nm $^{-1}$ spring constant under vertical DART-PFM mode to repeatedly scan a single 1 μ m 2 area (256 \times 256 pixels) at a fixed film thickness.

Phase Field Modeling: Phase-field modeling was used to simulate the polarization domains and their switching kinetics in (001) BFO nanopillars that were embedded in CFO matrix and grown on Nb-doped STO (Nb:STO) substrate. In the phase-field model of ferroelectrics, temporal evolution of spontaneous polarization $\mathbf{P} = (P_x, P_y, P_z)$ was governed by time-dependent Ginzburg-Landau (TDGL) equation, $\frac{\partial \mathbf{P}}{\partial \mathbf{t}} = -L \frac{\delta \mathbf{F}}{\delta \mathbf{P}}$, where L is kinetic coefficient; $F = \int_{\mathbf{V}} f_{\mathrm{tot}} \, \mathrm{d} x^3$ is total free energy, where the total free energy density $f_{\rm tot} = f_{\rm Landau} + f_{\rm gradient} + f_{\rm elastic} + f_{\rm electro}$ was contributed by following energy densities. The same as in Ref. [76], the expression of the Landau energy density was given as $f_{\text{Landau}} = \alpha_1(P_x^2 + P_y^2 + P_z^2) + \alpha_{11}(P_x^4 + P_y^4 + P_z^4) + \alpha_{12}(P_x^2 P_y^2 + P_y^2 P_z^2 + P_z^2 P_z^2),$ where α_1 , α_{11} and α_{12} are Landau-Devonshire coefficients; the gradient energy density $f_{\text{gradient}} = \frac{1}{2}G_{11}(\nabla P)^2$, where G_{11} is the isotropic gradient energy coefficient; the elastic energy density $f_{\text{elastic}} = \frac{1}{2} c_{ijkl} (\varepsilon_{ij} - \varepsilon_{ij}^0) (\varepsilon_{kl} - \varepsilon_{kl}^0)$, where c_{ijkl} (i, j, k, l = 1,2,3) are phase-dependent elastic stiffness coefficients, and the spatially variant total strain $oldsymbol{arepsilon}$ is obtained by solving mechanical equilibrium equation $\sigma=0$ with stress $\sigma_{ij}=c_{ijkl}(\varepsilon_{kl}-\varepsilon_{kl}^0)$. Here the eigenstrain $\varepsilon_{ii}^{0} = Q_{ijkl}P_{k}P_{l} + \varepsilon_{ii}^{mis}$ was contributed by electrostrictive strain with Q_{ijkl} (i, j, k, l = 1,2,3) being the electrostrictive coefficient, and by lattice mismatch strain $\varepsilon_{ii}^{\text{mis}}$ arising from both the BFO-CFO vertical interface and the BFO-Nb:STO horizontal interface. Based on the XRD analysis (Figure 1b), the ε_{zz}^{mis} was set to be positive (out-ofplane tensile normal strain) on the side of BFO and negative (out-ofplane compressive normal strain) on the side of CFO across the BFO/ CFO interface. The specific initial distribution of ε_{zz}^{mis} (see Section S7, Supporting Information) was tuned to ensure that the spatial profile of the $\langle \varepsilon_{77} \rangle$ at equilibrium, which was contributed by both the lattice mismatch at the BFO/CFO interface and the lattice deformation associated with the spontaneous polarization in the BFO, agrees with the values extracted from XRD. When solving $\nabla \cdot \sigma = 0$, stress continuity condition ($\sigma_{A} = \sigma_{B}$, A and B denotes different materials) was used at all interfaces between dissimilar materials. By setting the c_{iikl} of the air phase (above the VAN film) to be 0, the stress-free surface was automatically considered. The electrostatic energy density $f_{\text{electro}} = -\frac{1}{2} [\varepsilon_0 \varepsilon_r \mathbf{E} + \mathbf{P}] \cdot \mathbf{E}$, where $\mathbf{E} = \mathbf{E}_{d} + \mathbf{E}_{ext}$ is the total electric field, \mathbf{E}_{d} is the depolarization field, and \mathbf{E}_{ext} is the externally applied electric field. \mathbf{E}_{d} was obtained by solving the electrostatic equilibrium equation $\nabla \cdot \mathbf{D} = \nabla \cdot (\epsilon_0 \epsilon_r \mathbf{E}_d + \mathbf{P}) = 0$ where **D** is the electric displacement field, ε_0 is vacuum permittivity and ε_r is phase-dependent relative permittivity. For simplicity, polarization charges on all surfaces of the BFO nanopillar were assumed to be fully compensated because 1) Nb-doped STO substrate was electronically conductive; 2) the electronic conductivity of the CFO matrix was at the level of typical semiconductors; 3) the scanning tip during PFM imaging was in effect placing a metallic electrode on the top surface of the BFO. In this regard, when modeling polarization switching under positive bias voltage, a spatially uniform electric potential $\varphi=\varphi_0$ was applied on the top surface of VAN film while the Nb-doped STO substrate was grounded ($\varphi = 0$ V). As a result, the applied electric field can be approximated as $\mathbf{E}_{\text{ext}} = (0, 0, -\phi_0/d)$ with d being the thickness of the VAN

of polarization at electrical remanence. 3D discretized cells of $80\Delta x \times 80\Delta y \times 40\Delta z$ was employed to describe a multi-phase system (including the Nb:STO substrate, the BFO-CFO nanocomposite thin film, and the free space), where $\Delta x = \Delta y = \Delta z = 1$ mare cell size along x, y and z axes, respectively. Along the z-axis, the bottom 20 layers of cells $(20\Delta z)$ were designated as the Nb:STO substrate, the middle 10 layers $(10\Delta z)$ as the nanocomposite thin film, and the top 10 layers $(10\Delta z)$ as the free space. The profile of strain distribution in BFO nanopillar was largely same as that obtained from the simulations with the thickness of the Nb:STO substrate being $40\Delta z$. In the layers of BFO-CFO nanocomposite film, a cuboid-shaped BFO with a lateral size of $40\Delta x \times 40\Delta y$ was placed

film. The negative sign indicates that \mathbf{E}_{ext} was opposite to the direction

in the center of the film plane and embedded in the CFO matrix. For accelerating the computation, the size of the BFO nanopillar (40 nm \times 40 nm \times 10 nm) was scaled down by 5 times in simulation from the typical size of the BFO film in practice (200 nm \times 200 nm \times 50 nm). Since the aspect ratio remains unchanged, the profile of strain distribution remains unaffected (see Section S7, Supporting Information). Meanwhile, the isotropic gradient energy coefficient G_{11} was reduced (the energy penalty associated with the domain wall would then be reduced) to enable the formation of multiple ferroelectric domains in the BFO island as observed by PFM imaging (e.g., Figure 2d).

The material parameters that were used in the simulations were listed: for BFO, $\alpha_1(T)=4.9\times 10^5\times (T\text{-}1103)~\text{C}^{-2}~\text{m}^2~\text{N},~\alpha_{11}=6.5\times 10^8~\text{C}^{-4}~\text{m}^6~\text{N},~\alpha_{12}=1\times 10^8~\text{C}^{-4}~\text{m}^6~\text{N},~\text{and temperature}~T~\text{is in Kelvin.}$ $Q_{11}=0.032~\text{C}^{-2}~\text{m}^4,~Q_{12}=-0.016~\text{C}^{-2}~\text{m}^4,~\text{and}~Q_{44}=0.06~\text{C}^{-2}~\text{m}^4.$ The elastic stiffness coefficients $c_{11}=3\times 10^{11}~\text{Nm}^{-2},~c_{12}=1.62\times 10^{11}~\text{Nm}^{-2},~\text{and}~c_{44}=0.69\times 10^{11}~\text{Nm}^{-2}.$ The relative permittivity $\varepsilon_r=100.$ The isotropic gradient energy coefficient $G_{11}/G_{110}=0.03$ was chosen, where $\Delta x=\sqrt{G_{110}/\alpha_0}$ and $\alpha_0=|\alpha_1|_{T=298~\text{K}}.^{[76]}~\text{For CFO},~c_{11}=2.57\times 10^{11}~\text{Nm}^{-2},~c_{12}=1.5\times 10^{11}~\text{Nm}^{-2},~\text{and}~c_{44}=0.85\times 10^{11}~\text{Nm}^{-2}.^{[77]}~\text{The elastic stiffness}$ of STO was used for Nb:STO substrate, $c_{11}=3.17\times 10^{11}~\text{Nm}^{-2},~c_{12}=1.03\times 10^{11}~\text{Nm}^{-2},~\text{and}~c_{44}=1.24\times 10^{11}~\text{Nm}^{-2}.^{[78]}$ When numerically solving TDGL equation $\frac{\partial \mathbf{P}}{\partial \mathbf{t}}=-L\frac{\delta \mathbf{F}}{\delta \mathbf{P}},~\text{forward Euler}$

method was used for time-marching with a reduced time step $\Delta t^{*}=\alpha_0 L \Delta t=0.04$ and Δt is real-time step. Central finite difference was used for calculating spatial derivatives. The mechanical equilibrium equation $\nabla \cdot \sigma=0$ and electrostatic equilibrium equation $\nabla \cdot \sigma=0$ and electrostatic equilibrium equation $\nabla \cdot \sigma=0$ were numerically solved using the Fourier spectral iterative method (FSIM), [79] where the Fourier transformation was performed using the recently developed Parallel 3D Fast Fourier Transforms (P3DFFT) library [80] for obtaining high scaling performance in parallelization. This FSIM method, which was being used in the commercial phase-field-based simulation package μ-Pro (mupro.co), permits a fast and accurate solution of the aforementioned two equilibrium equations. The numerical accuracy of the in-house FSIM-based solvers was demonstrated through benchmarking test against the static electrostatic and elasticity solvers in COMSOL Multiphysics (see results in Section S8, Supporting Information).

Supporting Information

Supporting Information is available from the Wiley Online Library or from the author.

Acknowledgements

J.S. and B.D.H. recognize support from the Institute of Materials Science, University of Connecticut, and from the National Science Foundation (MRI development award, DMR-1726862). The work at Los Alamos National Laboratory was supported by the NNSA's Laboratory Directed Research and Development Program and was performed, in part, at the Center for Integrated Nanotechnologies, an Office of Science User Facility operated for the U.S. Department of Energy Office of Science. Los Alamos National Laboratory, an affirmative action equal opportunity employer, managed by Triad National Security, LLC for the U.S. Department of Energy's NNSA, under contract 89233218CNA000001. B.D.H is a CINT user and acknowledges the support from the CINT user program. J.H. acknowledges support from the National Science Foundation under award CBET-2006028. The phase-field simulations were performed in the Extreme Science and Engineering Discovery Environment (XSEDE), which is supported by National Science Foundation grant number ACI-1548562. Specifically, it used the Bridges-2 system, which is supported by NSF award number ACI-1445606, at the Pittsburgh Supercomputing Center (PSC).



www.afm-journal.de

Conflict of Interest

The authors declare no conflict of interest.

Data Availability Statement

The data that support the findings of this study are available from the corresponding author upon reasonable request.

Keywords

BiFeO₃-CoFe₂O₄, ferroelectric switching, interfacial strains, nanomachining, tomographic AFM

Received: March 8, 2021 Revised: May 7, 2021 Published online: June 17, 2021

- H. Zheng, J. Wang, S. E. Lofland, Z. Ma, L. Mohaddes-Ardabili,
 T. Zhao, L. Salamanca-Riba, S. R. Shinde, S. B. Ogale, F. Bai,
 D. Viehland, Y. Jia, D. G. Schlom, M. Wuttig, A. Roytburd,
 R. Ramesh, Science 2004, 303, 661.
- [2] N. M. Aimon, D. H. Kim, X. Sun, C. A. Ross, ACS Appl. Mater. Interfaces 2015, 7, 2263.
- [3] W. Zhang, M. Fan, L. Li, A. Chen, Q. Su, Q. Jia, J. L. MacManus-Driscoll, H. Wang, Appl. Phys. Lett. 2015, 107, 212901.
- [4] G. Tian, S. Ojha, S. Ning, X. Gao, C. A. Ross, Adv. Electron. Mater. 2019, 5, 1900012.
- [5] H. Zheng, F. Straub, Q. Zhan, P. L. Yang, W. K. Hsieh, F. Zavaliche, Y. H. Chu, U. Dahmen, R. Ramesh, Adv. Mater. 2006, 18, 2747.
- [6] D. H. Kim, N. M. Aimon, X. Sun, C. A. Ross, Adv. Funct. Mater. 2014, 24, 2334.
- [7] Y.-J. Chen, Y.-H. Hsieh, S.-C. Liao, Z. Hu, M.-J. Huang, W.-C. Kuo, Y.-Y. Chin, T.-M. Uen, J.-Y. Juang, C.-H. Lai, H.-J. Lin, C.-T. Chen, Y.-H. Chu, *Nanoscale* 2013, 5, 4449.
- [8] Z. Wang, Y. Yang, R. Viswan, J. Li, D. Viehland, Appl. Phys. Lett. 2011, 99, 043110.
- [9] Y.-H. Hsieh, J.-M. Liou, B.-C. Huang, C.-W. Liang, Q. He, Q. Zhan, Y.-P. Chiu, Y.-C. Chen, Y.-H. Chu, Adv. Mater. 2012, 24, 4564.
- [10] D. H. Kim, S. Ning, C. A. Ross, J. Mater. Chem. C 2019, 7, 9128.
- [11] W. Zhang, A. Chen, Z. Bi, Q. Jia, J. L. MacManus-Driscoll, H. Wang, Curr. Opin. Solid State Mater. Sci. 2014, 18, 6.
- [12] J. Ma, J. Hu, Z. Li, C.-W. Nan, Adv. Mater. 2011, 23, 1062.
- [13] A. Chen, Q. Su, H. Han, E. Enriquez, Q. Jia, Adv. Mater. 2019, 31, 1803241.
- [14] N. M. Aimon, H. K. Choi, X. Y. Sun, D. H. Kim, C. A. Ross, Adv. Mater. 2014, 26, 3063.
- [15] D. H. Kim, N. M. Aimon, C. A. Ross, APL Mater. 2014, 2, 081101.
- [16] R. Comes, H. Liu, M. Khokhlov, R. Kasica, J. Lu, S. A. Wolf, *Nano Lett.* 2012, 12, 2367.
- [17] S. M. Stratulat, X. Lu, A. Morelli, D. Hesse, W. Erfurth, M. Alexe, Nano Lett. 2013, 13, 3884.
- [18] S.-H. Baek, S. Choi, T. L. Kim, H. W. Jang, Curr. Appl. Phys. 2017, 17, 688.
- [19] B. J. Rodriguez, S. Jesse, A. P. Baddorf, T. Zhao, Y. H. Chu, R. Ramesh, E. A. Eliseev, A. N. Morozovska, S. V. Kalinin, Nanotechnology 2007, 18, 405701.
- [20] F. Zavaliche, T. Zhao, H. Zheng, F. Straub, M. P. Cruz, P. L. Yang, D. Hao, R. Ramesh, Nano Lett. 2007, 7, 1586.
- [21] H. T. Chen, L. Hong, A. K. Soh, J. Appl. Phys. 2011, 109, 094102.

- [22] J. L. MacManus-Driscoll, P. Zerrer, H. Wang, H. Yang, J. Yoon, A. Fouchet, R. Yu, M. G. Blamire, Q. Jia, Nat. Mater. 2008, 7, 314.
- [23] A. Chen, J.-M. Hu, P. Lu, T. Yang, W. Zhang, L. Li, T. Ahmed, E. Enriquez, M. Weigand, Q. Su, H. Wang, J.-X. Zhu, J. L. MacManus-Driscoll, L.-Q. Chen, D. Yarotski, Q. Jia, Sci. Adv. 2016, 2, e1600245.
- [24] F. Zavaliche, H. Zheng, L. Mohaddes-Ardabili, S. Y. Yang, Q. Zhan, P. Shafer, E. Reilly, R. Chopdekar, Y. Jia, P. Wright, D. G. Schlom, Y. Suzuki, R. Ramesh, *Nano Lett.* 2005, 5, 1793.
- [25] T. Amrillah, Y. Bitla, K. Shin, T. Yang, Y.-H. Hsieh, Y.-Y. Chiou, H.-J. Liu, T. H. Do, D. Su, Y.-C. Chen, S.-U. Jen, L.-Q. Chen, K. H. Kim, J.-Y. Juang, Y.-H. Chu, ACS Nano 2017, 11, 6122.
- [26] D. Sando, B. Xu, L. Bellaiche, V. Nagarajan, Appl. Phys. Rev. 2016, 3, 011106.
- [27] Y. Yang, I. C. Infante, B. Dkhil, L. Bellaiche, C. R. Phys. 2015, 16, 193.
- [28] H. Guo, R. Zhao, K.-j. Jin, L. Gu, D. Xiao, Z. Yang, X. Li, L. Wang, X. He, J. Gu, Q. Wan, C. Wang, H. Lu, C. Ge, M. He, G. Yang, ACS Appl. Mater. Interfaces 2015, 7, 2944.
- [29] A. Chen, Y. Dai, A. Eshghinejad, Z. Liu, Z. Wang, J. Bowlan, E. Knall, L. Civale, J. L. MacManus-Driscoll, A. J. Taylor, R. P. Prasankumar, T. Lookman, J. Li, D. Yarotski, Q. Jia, Adv. Sci. 2019, 6, 1901000.
- [30] M. D. Biegalski, D. H. Kim, S. Choudhury, L. Q. Chen, H. M. Christen, K. Dörr, Appl. Phys. Lett. 2011, 98, 142902.
- [31] D. H. Kim, H. N. Lee, M. D. Biegalski, H. M. Christen, Appl. Phys. Lett. 2008, 92, 012911.
- [32] Y. Tong, M. Liu, H. M. Chen, G. P. Li, H. Fang, J. Wang, Z. Ma, J. Appl. Phys. 2015, 117, 074102.
- [33] H. W. Jang, S. H. Baek, D. Ortiz, C. M. Folkman, R. R. Das, Y. H. Chu, P. Shafer, J. X. Zhang, S. Choudhury, V. Vaithyanathan, Y. B. Chen, D. A. Felker, M. D. Biegalski, M. S. Rzchowski, X. Q. Pan, D. G. Schlom, L. Q. Chen, R. Ramesh, C. B. Eom, *Phys. Rev. Lett.* 2008, 101, 107602.
- [34] S. Choudhury, Y. L. Li, L. Q. Chen, Q. X. Jia, Appl. Phys. Lett. 2008, 92, 142907.
- [35] N. Dix, R. Muralidharan, J. Guyonnet, B. Warot-Fonrose, M. Varela, P. Paruch, F. Sánchez, J. Fontcuberta, Appl. Phys. Lett. 2009, 95, 062007
- [36] M. Tyagi, M. Kumari, R. Chatterjee, P. Sharma, Phys. B 2014, 448, 128.
- [37] J. L. MacManus-Driscoll, Adv. Funct. Mater. 2010, 20, 2035.
- [38] M. Chen, J. Ma, R.-C. Peng, Q. Zhang, J. Wang, Y. Liang, J. Wu, L.-Q. Chen, J. Ma, C.-W. Nan, Acta Mater. 2019, 175, 324.
- [39] J. Ma, J. Ma, Q. Zhang, R. Peng, J. Wang, C. Liu, M. Wang, N. Li, M. Chen, X. Cheng, P. Gao, L. Gu, L.-Q. Chen, P. Yu, J. Zhang, C.-W. Nan, Nat. Nanotechnol. 2018, 13, 947.
- [40] A. K. Yadav, C. T. Nelson, S. L. Hsu, Z. Hong, J. D. Clarkson, C. M. Schlepütz, A. R. Damodaran, P. Shafer, E. Arenholz, L. R. Dedon, D. Chen, A. Vishwanath, A. M. Minor, L. Q. Chen, J. F. Scott, L. W. Martin, R. Ramesh, *Nature* 2016, 530, 198.
- [41] M. J. Han, Y. L. Tang, Y. J. Wang, Y. L. Zhu, J. Y. Ma, W. R. Geng, Y. P. Feng, M. J. Zou, N. B. Zhang, X. L. Ma, Acta Mater. 2020, 187, 12.
- [42] M.-J. Han, Y.-J. Wang, Y.-L. Tang, Y.-L. Zhu, J.-Y. Ma, W.-R. Geng, M.-J. Zou, Y.-P. Feng, N.-B. Zhang, X.-L. Ma, J. Phys. Chem. C 2019, 123, 2557.
- [43] F. Hui, C. Wen, S. Chen, E. Koren, R. Dechter, D. Lewis, M. Lanza, Adv. Funct. Mater. 2020, 30, 1902776.
- [44] F. Zhang, D. Edwards, X. Deng, Y. Wang, J. I. Kilpatrick, N. Bassiri-Gharb, A. Kumar, D. Chen, X. Gao, B. J. Rodriguez, J. Appl. Phys. 2020, 127, 034103.
- [45] B. D. Huey, Annu. Rev. Mater. Res. 2007, 37, 351.
- [46] R. K. Vasudevan, N. Balke, P. Maksymovych, S. Jesse, S. V. Kalinin, Appl. Phys. Rev. 2017, 4, 021302.
- [47] C. Canale, B. Torre, D. Ricci, P. C. Braga, In Recognizing and Avoiding Artifacts in Atomic Force Microscopy Imaging, Vol. 736, Humana Press, Totowa, NJ 2011.



www.afm-journal.de

- [48] J. J. Steffes, R. A. Ristau, R. Ramesh, B. D. Huey, Proc. Natl. Acad. Sci. USA 2019, 116, 2413.
- [49] J. Luria, Y. Kutes, A. Moore, L. Zhang, E. A. Stach, B. D. Huey, Nat. Energy 2016, 1, 16150.
- [50] J. Song, Y. Zhou, N. P. Padture, B. D. Huey, Nat. Commun. 2020, 11, 3308.
- [51] J. Song, Y. Zhou, B. D. Huey, Appl. Phys. Lett. 2021, 118, 080501.
- [52] B. D. Huey, R. Nath Premnath, S. Lee, N. A. Polomoff, J. Am. Ceram. Soc. 2012, 95, 1147.
- [53] R. W. Cheary, A. Coelho, J. Appl. Crystallogr. 1992, 25, 109.
- [54] L. Zhang, Y. Yuan, J. Lapano, M. Brahlek, S. Lei, B. Kabius, V. Gopalan, R. Engel-Herbert, ACS Nano 2018, 12, 1306.
- [55] A. I. Klyndyuk, E. A. Chizhova, Inorg. Mater. 2015, 51, 272.
- [56] J. D. Bucci, B. K. Robertson, W. J. James, J. Appl. Crystallogr. 1972, 5, 187.
- [57] Z. H. Bi, J. H. Zhu, J. L. Batey, J. Power Sources 2010, 195, 3605.
- [58] D. de Ligny, P. Richet, Phys. Rev. B 1996, 53, 3013.
- [59] Y.-C. Chen, G.-F. Wang, H.-H. Tai, J.-W. Chen, Y.-C. Huang, J.-C. Yang, Y.-H. Chu, Nanotechnology 2011, 22, 254030.
- [60] T. Zhao, A. Scholl, F. Zavaliche, K. Lee, M. Barry, A. Doran, M. P. Cruz, Y. H. Chu, C. Ederer, N. A. Spaldin, R. R. Das, D. M. Kim, S. H. Baek, C. B. Eom, R. Ramesh, Nat. Mater. 2006, 5, 823.
- [61] H. Huyan, L. Li, C. Addiego, W. Gao, X. Pan, Natl. Sci. Rev. 2019, 6,
- [62] Y.-H. Chu, Q. He, C.-H. Yang, P. Yu, L. W. Martin, P. Shafer, R. Ramesh, Nano Lett. 2009, 9, 1726.
- [63] R. N. Torah, S. P. Beeby, N. M. White, J. Phys. D: Appl. Phys. 2004, *37*, 1074.
- [64] A. Almusallam, K. Yang, D. Zhu, R. N. Torah, A. Komolafe, J. Tudor, S. P. Beeby, Smart Mater. Struct. 2015, 24, 115030.

- [65] B. S. Lang, IEEE Trans. Dielectr. Electr. Insul. 2004, 11, 3.
- [66] C. Pham, A. Petre, L. Berquez, R. Flores-Suarez, A. Mellinger, W. Wirges, R. Gerhard, IEEE Trans. Dielectr. Electr. Insul. 2009, 16, 676.
- [67] A. Gruverman, M. Alexe, D. Meier, Nat. Commun. 2019, 10, 1661.
- [68] (Eds: S. V. Kalinin, A. Gruverman), Scanning Probe Microscopy of Functional Materials, Springer-Verlag, New York 2011.
- [69] J. T. Heron, J. L. Bosse, Q. He, Y. Gao, M. Trassin, L. Ye, J. D. Clarkson, C. Wang, J. Liu, S. Salahuddin, D. C. Ralph, D. G. Schlom, J. Íñiguez, B. D. Huey, R. Ramesh, Nature 2014, 516, 370.
- [70] S. Hu, A. Alsubaie, Y. Wang, J. H. Lee, K. R. Kang, C. H. Yang, J. Seidel, Phys. Status Solidi 2017, 214, 1600356.
- [71] Z. Wen, X. Qiu, C. Li, C. Zheng, X. Ge, A. Li, D. Wu, Appl. Phys. Lett. 2014, 104, 042907.
- [72] P. Gao, C. T. Nelson, J. R. Jokisaari, S.-H. Baek, C. W. Bark, Y. Zhang, E. Wang, D. G. Schlom, C.-B. Eom, X. Pan, Nat. Commun. 2011, 2, 591.
- [73] S. Jesse, B. J. Rodriguez, S. Choudhury, A. P. Baddorf, I. Vrejoiu, D. Hesse, M. Alexe, E. A. Eliseev, A. N. Morozovska, J. Zhang, L.-Q. Chen, S. V. Kalinin, Nat. Mater. 2008, 7, 209.
- [74] A. Gruverman, D. Wu, J. F. Scott, Phys. Rev. Lett. 2008, 100, 097601.
- [75] J.-M. Hu, L.-Q. Chen, C.-W. Nan, Adv. Mater. 2016, 28, 15.
- [76] S. H. Baek, H. W. Jang, C. M. Folkman, Y. L. Li, B. Winchester, J. X. Zhang, Q. He, Y. H. Chu, C. T. Nelson, M. S. Rzchowski, X. Q. Pan, R. Ramesh, L. Q. Chen, C. B. Eom, Nat. Mater. 2010, 9, 309.
- [77] Z. Li, E. S. Fisher, J. Z. Liu, M. V. Nevitt, J. Mater. Sci. 1991, 26, 2621.
- [78] R. O. Bell, G. Rupprecht, Phys. Rev. 1963, 129, 90.
- [79] J. J. Wang, X. Q. Ma, Q. Li, J. Britson, L.-Q. Chen, Acta Mater. 2013, 61, 7591.
- [80] D. Pekurovsky, SIAM Journal on Scientific Computing 2012, 34,